Dalton Transactions

Cite this: *Dalton Trans.*, 2012, **41**, 4544

www.rsc.org/dalton

PAPER

Water-soluble Fe_3O_4 nanoparticles with high solubility for removal of heavy-metal ions from waste water

Lixia Wang,[a,b] Jianchen Li,[a] Qing Jiang[a] and Lijun Zhao*[a]

Received 27th September 2011, Accepted 6th January 2012
DOI: 10.1039/c2dt11827k

In this contribution, we synthesized water-soluble Fe_3O_4 nanoparticles (NPs) with sufficiently high solubility (28 mg mL^{-1}) and stability (at least one month) through a hydrothermal approach, and found that they exhibited excellent removal ability for heavy-metal ions from waste water. For the first time, the water-soluble Fe_3O_4 NPs were used as adsorbents for heavy-metals removal from wastewater. It is noteworthy that the adsorption ability of the water-soluble Fe_3O_4 NPs for Pb^{2+} and Cr^{6+} is stronger than water-insoluble Fe_3O_4 NPs. Furthermore, the water-soluble Fe_3O_4 NPs exhibited relatively high saturation magnetization (83.4 emu g^{-1}), which allowed their highly-efficient magnetic separation from wastewater. The most important thing is that the water-soluble magnetite as an adsorbent can directly dissolve in water without the help of mechanical stirring or any extraneous forces, which may solve a key problem for the practical application of magnetic powders in the field of sewage purification. Moreover, the water-soluble Fe_3O_4 NPs show a highly-efficient adsorption capacity for 10 ppm of Pb^{2+} ions solution which can reach 90% within 2 minutes.

Introduction

Contamination of heavy-metals in water supplies has steadily increased over the last years as a result of over population and expansion of industrial activities. Metal pollution has a harmful effect on biological systems and does not undergo biodegradation. For example, Pb^{2+} can obstruct heme biosynthesis, inhibit several zinc enzymes, interact with nucleic acids and tRNA to affect protein synthesis, and accumulate in the apatite structure of bone.[1] Cr^{6+} is widely used in a variety of industries such as stainless steel, textile dyes, wood preservation and leather tanning. This heavy-metal is recognized as a human genotoxic carcinogen that can be easily absorbed into the body through the digestive system, respiratory tract and skin contact.[2] Therefore, the elimination of toxic metals from aqueous solutions is important for the protection of public health. Although a lot of methods, such as chemical precipitation, ion exchange, liquid–liquid extraction, resins, cementation, and electrodialysis have been developed for the extraction of the above heavy-metal ions from industrial wastewater.[3] However, from a practical point of view, the application of such adsorbents for treating wastewater has a major drawback, which is that it requires an additional separation step to remove the adsorbent from the solution. One of the new developments for removing heavy-metal ions from wastewater in recent years is to use magnetite as adsorbents, due to its high adsorption capacity for heavy-metals and organic pollutants.[4] The most important advantage of using Fe_3O_4 as adsorbents or magnetic supports of catalysts is that it can be easily separated from the reaction system with an external magnetic field.

However, for the practical application of magnetic powders as adsorbents, there is still a great challenge to solve the dispersibility of magnetic powders into the sewage water without any extraneous forces.[5] Herein, we show how Fe_3O_4 NPs with large solubility and high stability in water can be synthesized in large amounts. These water-soluble Fe_3O_4 NPs were used as a fast recyclable tool for Pb^{2+} and Cr^{6+} removal from sewage water for the first time. The mechanism for adsorption of Pb^{2+} and Cr^{6+} was also discussed. It is noteworthy that the adsorption ability of the water-soluble Fe_3O_4 NPs to Pb^{2+} and Cr^{6+} is stronger than water-insoluble Fe_3O_4 NPs. In summary, water-soluble iron oxide NPs can be directly dissolved and well stabilized in sewage water, and then an effective magnetic separation was used to call back the absorbent after complete adsorption.

Materials and methods

All chemicals were of analytical grade and were used without further purification. The chemicals were obtained from Beijing Chemicals Co. (Beijing, China).

Preparation of water-soluble Fe_3O_4 nanoparticles

The water-soluble Fe_3O_4 NPs were prepared by the conventional one-pot hydrothermal method. In a typical synthesis, 0.540 g

[a]*Key Laboratory of Automobile Materials, Ministry of Education and School of Materials Science and Engineering, Jilin University, Changchun130022, China*
[b]*School of Mechanical Science and Engineering, Northeast Petroleum University, Daqing163318, China. E-mail: lijunzhao@jlu.edu.cn; Fax: +(86)431-85095876; Tel: +(86)431-85095878*

(2 mmol) of $FeCl_3 \cdot 6H_2O$ and 1.176 g (4 mmol) sodium citrate were dissolved in 40 mL of distilled water. Then 0.5 mL of ammonia (13.2 mol L^{-1}) and 0.3 g of polyacrylamide (PAM) were added to the solution at room temperature with simultaneous vigorous agitation. The mixtures were stirred vigorously for 30 minutes and then sealed in a Teflon-lined stainless-steel autoclave and maintained at 200 °C for 12 hours. After completion of the reaction, the solid product was collected by magnetic filtration and washed several times with deionized water and absolute ethanol. The final product was dried in a vacuum oven at 100 °C for 6 hours. Water-soluble Fe_3O_4 NPs were obtained and characterized as S1. If the dosage of PAM was reduced to 0.05 g while other conditions were kept the same, water-soluble Fe_3O_4 NPs were obtained and characterized as S2.

Preparation of water-insoluble Fe_3O_4 nanoparticles

In order to compare the adsorption capacity of water-soluble and water-insoluble Fe_3O_4 NPs for heavy-metal ions, water-insoluble Fe_3O_4 NPs were prepared and characterized as S3, which had similar a particle size to S1 and S2. Briefly, 0.200 g (0.740 mmol) of $FeCl_3 \cdot 6H_2O$ and 0.500 g (1.7 mmol) of sodium citrate were dissolved in 20 mL of distilled water. Then 3.0 mL of ethylenediamine (15.0 mol L^{-1}) was added under continuous stirring until it had fully dissolved. The solution was transferred to a Teflon-lined autoclave. The autoclave was then sealed ad maintained at 200 °C for 12 hours; the other conditions were kept the same.

Characterization methods

The phases were identified by means of X-ray diffraction (XRD) with a Rigaku D/max 2500pc X-ray diffractometer with Cu Kα radiation (λ) 1.54156 Å at a scan rate of 0.02° s^{-1}; morphologies were characterized using a JEOL JSM-6700F field emission scanning electron microscopy (FESEM) operated at an acceleration voltage of 8.0 kV. IR spectra of the samples were obtained using a FTIR spectrophotometer (NEXUS, 670) in KBr pellets. Hysteresis loops were measured on a VSM-7300 vibrating sample magnetometer (VSM) (Lakeshore, USA) at room temperature. N_2 adsorption–desorption isotherms were measured at the temperature of liquid nitrogen (77 K) using a JW analyzer (JW-RB224, Beijing). Samples were degassed at 120°C overnight before measurements. Specific surface areas were calculated using the Brunauer–Emmett–Teller (BET) model. The concentration of Cr^{6+} and Pb^{2+} in all samples was measured using atomic absorption spectroscopy (AAS) (TAS-986, Beijing).

Batch adsorption experiments

Standard stock solutions of Pb^{2+} and Cr^{6+} (1 g L^{-1}) were prepared by dissolving spectrometrically pure $Pb(NO_3)_2$ and $K_2Cr_2O_7$, respectively. The stock solution of Pb^{2+} and Cr^{6+} (1 g L^{-1}) was prepared in deionized water and the desired concentrations of metal ions were obtained by diluting the same with water. The calibration curve of Pb^{2+} and Cr^{6+} was prepared by measuring the absorbance of different predetermined concentrations of the samples using atomic absorption spectroscopy (AAS) at λ_{max} = 283.3 nm and λ_{max} = 357.9 nm, respectively. Then, the adsorbent was added to the above solutions. After reaching adsorption equilibrium, Fe_3O_4 NPs were magnetically separated from the aqueous solution and the residual concentrations of metal ions in the aliquot were determined by AAS. The amount of heavy-metal ions adsorbed per unit mass of adsorption (mg g^{-1}) at equilibrium concentration, q_e, was calculated according to the equation:

$$q_e = \frac{(C_0 - C_e) \times V}{W} \quad (1)$$

where C_0 is the initial concentration of metal ion, mg dm^{-3}; C_e is the equilibrium concentration in solution, mg dm^{-3}; V is the total volume of solution, dm^3, and W is the dry weight of the hydrogel beads, g.

Results and discussion

Characterization of Fe_3O_4 nanoparticles

The SEM image (Fig. 1a) shows that product S1 consists of well dispersed spheres. Their particle sizes are in the range of 100–130 nm. In the high-magnification SEM image (Fig. 1b), a great number of cracks on the surface of the spheres can be clearly observed. It can be clearly observed that the hollow sphere is composed of shaped primary particles with a size of approximately 20 nm. The low-magnification SEM image of S2, as shown in Fig. 1c, shows that their particle sizes are in the range of 120–140 nm. In the SEM image of S2 at high magnification (Fig. 1d), the hollow sphere is composed of shaped primary particles with a size of approximately 25 nm. The increase of the particle size of S2 may be associated with the decreasing viscosity of the reaction solution. In our synthesis, when the concentration of the PAM is decreased from 0.3 to 0.05 g, the viscosity of the solution apparently declines. The decreased viscosity will accelerate the reaction rate as well as the movement rate of primary nanoparticles.[6] Uniform nanoparticles of S3 with particle sizes of around 25 nm are observed in Fig. 1e.

Fig. 1f shows the XRD patterns of S1–S3. All the diffraction peaks can be indexed to the face-centered cubic structure of magnetite according to JCPDS card No. 19-0629. The diffraction peaks at 2θ values of 30.10°, 35.45°, 37.01°, 43.09°, 53.46°, 56.98°, 62.75° and 65.79° can be ascribed to the reflection of the (220), (311), (222), (400), (422), (511), (440) and (533) planes of the cubic Fe_3O_4, respectively. The strong and sharp peaks indicate that S1, S2 and S3 are well crystallized. No peaks from other phases are detected, indicating the high purity of the products.

Well water-soluble Fe_3O_4 NPs were prepared using a facile one-step method. The synthesized magnetite samples show high water solubility (28 mg L^{-1}) at laboratory temperature (18 °C) and stability (at least 1 month), and they exhibit a rapid response to an external magnetic field. Take S1 as an example: Fig. 1g shows in photographs that S1 NPs are well dissolved in aqueous solution. Then, the magnetic powders dissolved in water are attracted by a magnet in 1 second. Subsequently, the particles are all stuck to the vial wall within 2 minutes. After taking off the

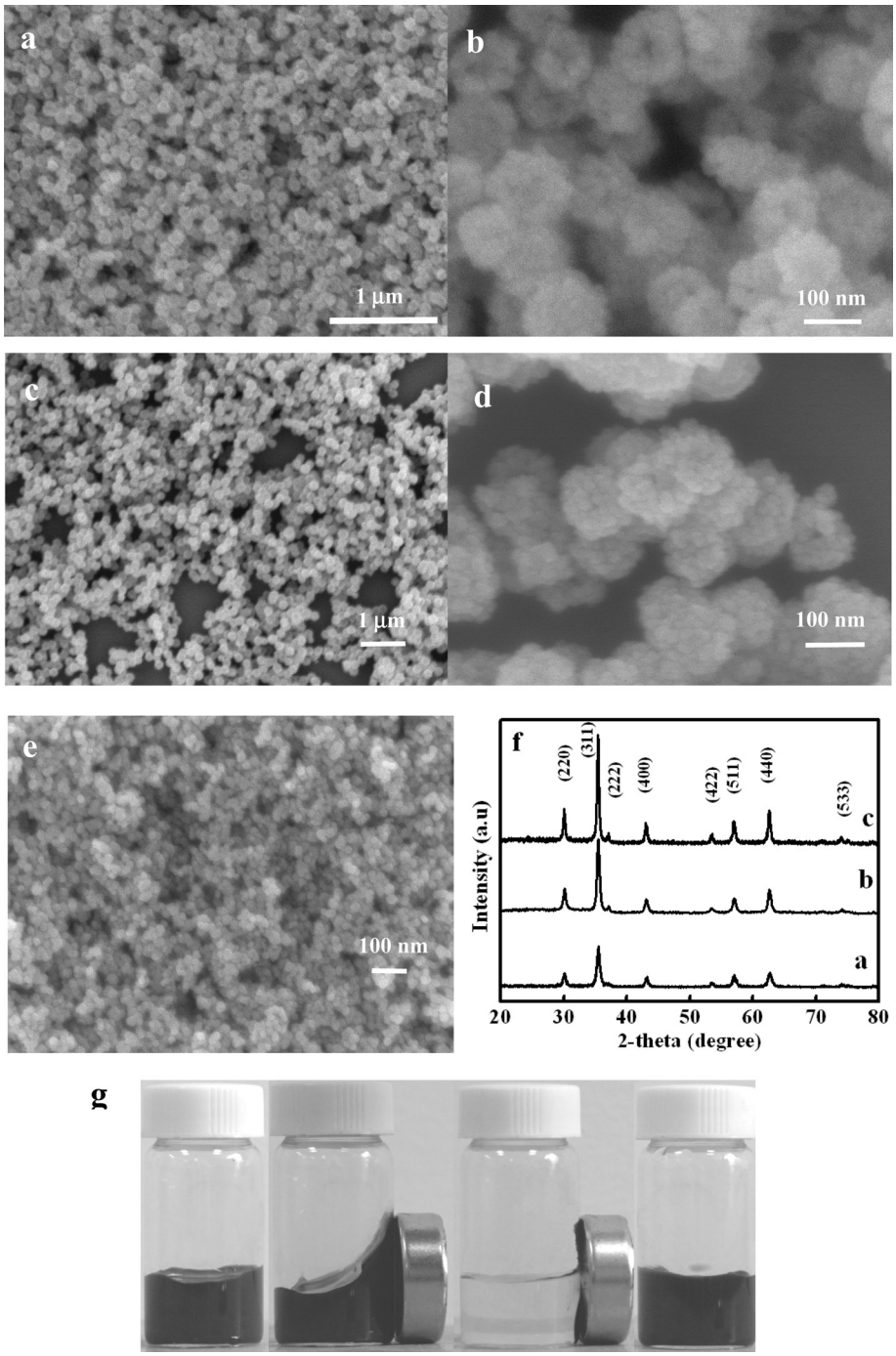

Fig. 1 SEM images of (a) low- and (b) high-magnification S1; SEM images of (c) low- and (d) high-magnification S2; (e) SEM images of S3; (f) XRD patterns of: a) S1, b) S3 and c) S2; (g) photos of S1 dissolved into water and separated by a magnet.

magnet, the magnetite particles will be re-dissolved into the aqueous solution by a slight shake.

As far as is known, citrate is an effective surfactant for the preparation of water-soluble magnetic powders due to the charge of citrate ions.[5b,7] FTIR analysis was also performed to reveal the surface nature of S1, S1 after adsorption, and sodium citrate, as shown in Fig. 2A. The spectra display a broad band at 580 cm^{-1}, which is believed to be associated with the stretching vibrations of the tetrahedral groups (Fe^{3+}–O^{2-}) for Fe_3O_4.[7] A broad band at around 3436 cm^{-1} corresponds to O–H stretching vibration of citrate and absorbed water molecules. Peaks corresponding to stretching modes ν(asymmetrical, COO^-), ν(symmetrical, COO^-) and ν(CH) of citrate appeared at 1629, 1383 and 1054 cm^{-1}, respectively, observed in parts of Fig. 2A, indicate that the citrate molecules have been adsorbed on the surface of NPs. Compared with FTIR spectroscopy of sodium citrate in Fig. 2A-c (red line), the citrate molecules have been obviously adsorbed on the surface of NPs. Fig. 2A-b shows the

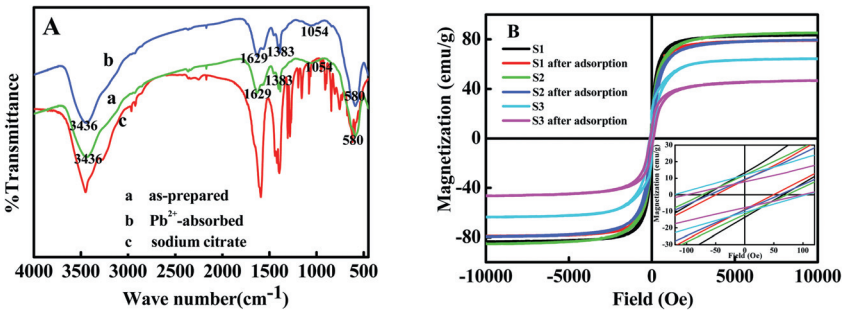

Fig. 2 (A) FTIR spectra of (a) S1, (b) S1 loaded with Pb^{2+} ions and (c) sodium citrate. (B) Magnetization curves of S1 to S3 measured at room temperature before and after adsorption.

Table 1 Magnetic parameters of S1 to S3 before and after adsorption at room temperature

Samples	M_s (emu g^{-1})	M_r (emu g^{-1})	H_c (Oe)
S1	83.4 ± 0.1	13.3 ± 0.1	66.4 ± 0.1
After adsorption	79.1 ± 0.1	8.9 ± 0.1	49.4 ± 0.1
S2	85.2 ± 0.1	12.0 ± 0.1	72.7 ± 0.1
After adsorption	79.4 ± 0.1	9.4 ± 0.1	60.8 ± 0.1
S3	64.1 ± 0.1	11.9 ± 0.1	106.6 ± 0.1
After adsorption	46.7 ± 0.1	7.8 ± 0.1	98.7 ± 0.1

curves of S1 after adsorption. Fig. 2A-a and A-b have a similar trend, which reveals the citrate ions are immobilized on the surface of nanoparticles after adsorption. The hydrophilic group of citrate provides an important role in the preparation of water-soluble Fe_3O_4 nanoparticles. During the hydrothermal process, citrate ions are immobilized on the nanoparticle surface, there are three carboxyl groups in every citrate ion, and the repulsive forces between the electric charges of the radical ions make the Fe_3O_4 NPs dissolve well in water.[12]

Magnetic properties

The magnetic properties of magnetic absorbents directly influence the callback efficiency. Hence, excellent magnetic performance is also a key role for the magnetic material as magnetic absorbent. Here, the magnetism of S1–S3 before and after adsorption is evaluated.

The room-temperature hysteresis loops of S1–S3 before and after adsorption were shown in Fig. 2B. Furthermore, the magnetic parameters of the samples obtained from hysteresis loops were listed in Table 1. The test results show that for S1–S3 after adsorption the saturation magnetization (M_s) values of magnetite decreased to some extent. It must be acknowledged that the adsorbents after adsorption still have high M_s values, especially the water-soluble products (S1 and S2). The relatively high M_s values (before and after adsorption) of the water-soluble magnetite nanoparticles facilitate the quick removal and callback of heavy-metal ions.

Environmental application for heavy-metal remediation

The three samples were directly dissolved in a certain amount of sewage water including Cr^{6+} and Pb^{2+} ions, respectively.

Removal of Pb^{2+}

The schemes for the removal of Pb^{2+} from aqueous solution using S1–S3 as adsorbents are shown in Fig. 3. The effects of contact time on the adsorption process were studied in the time range from 0 to 90 min at pH = 7.0, and 18 ± 1 °C with a fixed adsorbent dose. For the three metal concentrations studied, it was observed that the adsorption increased with increasing contact time. The adsorption increased rapidly during the first 10 min, then it was moderate up to 30 min, and thereafter the adsorption remained constant. According to the results as shown in Fig. 3, the time to reach equilibrium was 60 min with high concentrations of heavy-metal ions.

The effect of the concentration of Pb^{2+} was investigated by repeating experiments with different initial concentrations (10, 50 and 100 mg L^{-1}) of Pb^{2+} ions. Fig. 3 reveals the dependence of the adsorption capacity of Pb^{2+} ions on the concentration. When the initial Pb^{2+} ions concentration varied from 10 to 100 mg L^{-1}, the adsorption capacity of S1, S2 and S3 increased from 88.1 to 96.8 mg g^{-1}, 69.9 to 81.9 mg g^{-1}, and 45.0 to 61.8 mg g^{-1}, respectively. An exciting experimental result was obtained that the adsorption capacities of the water-soluble Fe_3O_4 NPs for Pb^{2+} ions are larger than that of water-insoluble Fe_3O_4 NPs. Especially, S1 exhibits the maximum adsorption capacity. The adsorption capacity of S1 for Pb^{2+} ions is calculated to be 96.8 mg g^{-1}, which is far higher than that of S3 (61.8 mg g^{-1}). This result shows that the water-soluble Fe_3O_4 NPs can treat wastewater with high concentrations of heavy-metal ions.

Adsorption isotherms

Analysis of adsorption isotherms is of fundamental importance to describe how adsorbate molecules interact with the adsorbent surface. The data of Pb^{2+} adsorption were fitted with Freundlich[8] and Langmuir[9] isotherm models.

The Freundlich adsorption isotherm can be expressed as:

$$\log q_e = \log K_F + \frac{1}{n}\log C_e \quad (2)$$

where K_F and n are the Freundlich adsorption isotherm constants, being indicative of the extent of the adsorption and the degree of nonlinearity between solution concentration and adsorption, respectively. K_F and $1/n$ values can be calculated

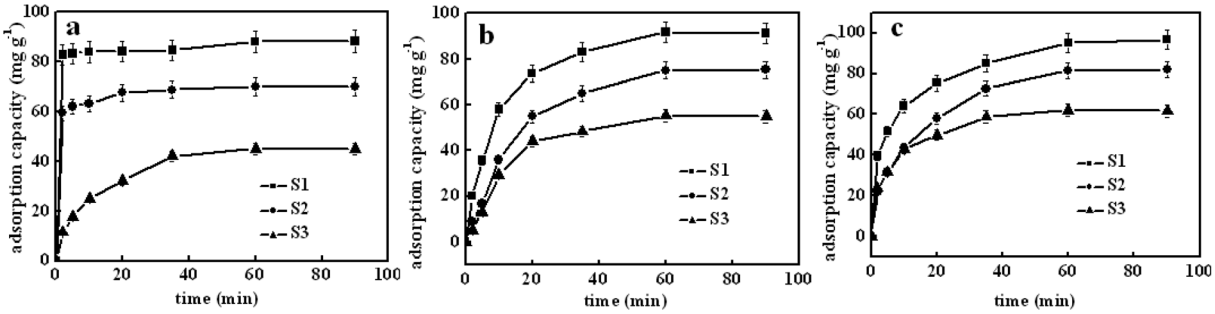

Fig. 3 The adsorption capacity of S1, S2 and S3 for (a) 10 mg L^{-1} of Pb^{2+}, (b) 50 mg L^{-1} of Pb^{2+} and (c) 100 mg L^{-1} of Pb^{2+}.

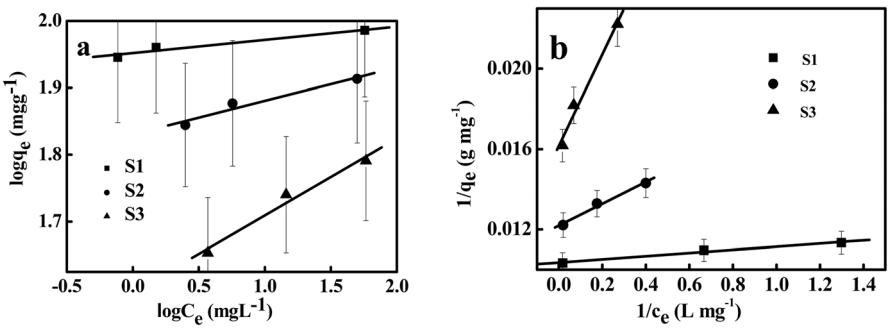

Fig. 4 Adsorption isotherms for adsorption of Pb^{2+} on Fe_3O_4 NPs (15 mg of adsorbent) (a) Freundlich model and (b) Langmuir model.

from the intercept and slope of the linear plot between log C_e and log q_e.

The Langmuir isotherm is expressed as:

$$\frac{1}{q_e} = \frac{1}{q_{max}} + \frac{1}{K_L q_{max}} \frac{1}{C_e} \quad (3)$$

where q_{max} is the maximum amount of adsorption with complete monolayer coverage on the adsorbent surface (mg g^{-1}), and K_L is the Langmuir constant related to the energy of adsorption (L mg^{-1}). The Langmuir constants K_L and q_{max} can be determined from the linear plot of $1/C_e$ *versus* $1/q_e$.

The essential characteristics of the Langmuir isotherm can be expressed by a dimensionless constant called the equilibrium parameter R_L that is defined by the following equation:

$$R_L = \frac{1}{(1 + K_L C_0)} \quad (4)$$

where K_L and C_0 are the same as defined before. The value of R_L is calculated from the above expression. The nature of the adsorption process is either unfavorable ($R_L > 1$), linear ($R_L = 1$), favorable ($0 < R_L < 1$) or irreversible ($R_L = 0$).

The Freundlich isotherm was employed to describe heterogeneous systems and reversible adsorption, which is not restricted to monolayer formations. Unlike the Freundlich isotherm, the Langmuir isotherm is based on the assumption that the structure of the adsorbent is homogeneous, where all sorption sites are identical and energetically equivalent.

Fig. 4a and b represent plots of the experimental data based on Freundlich and Langmuir isotherm models, respectively. Table 2 shows the calculated values of the Freundlich and Langmuir model's parameters. The comparison of correlation coefficients (r^2) of the linearized form of both equations indicates that the Langmuir model yields a better fit for the experimental equilibrium adsorption data than the Freundlich model. This suggests monolayer coverage of the surface of Fe_3O_4 NPs by Pb^{2+}. The maximum adsorption capacity (q_{max}) for Pb^{2+} is shown in Table 2. A good agreement with this adsorption model is confirmed by the similar values of calculated q_{max} and the experimental ones for adsorbent. Here, R_L-values obtained are listed in Table 2. All the R_L-values for the adsorption of Pb^{2+} onto Fe_3O_4 NPs are in the range of 0–1, indicating that the adsorption process is favorable.

Adsorption kinetics

The adsorption kinetic models were applied to interpret the experimental data to determine the controlling mechanism of Pb^{2+} adsorptions from aqueous solution. Here, pseudo-first-order, pseudo-second-order and the intraparticle diffusion models were used to test dynamical experimental data.

The pseudo-first-order kinetic model of Lagergren[10] is given by:

$$\log(q_{1e} - q_t) = \log q_{1e} - \frac{K_1 t}{2.303} \quad (5)$$

where q_t is the amount of Pb^{2+} adsorbed per unit of adsorbent (mg g^{-1}) at time t, K_1 is the pseudo-first-order rate constant

Table 2 Adsorption isothermal constants calculated from Langmuir and Freundlich models

	Langmuir model					Freundlich model			
Adsorbent	q_{max} (mg g^{-1})	K_L (L mg^{-1})	r_L^2	R_L	SD	K_F (mg$^{1-1/n}$ L$^{1/n}$ g^{-1})	N	r_F^2	SD
S1	96.6	13.15	0.9838	0–1	9.1E-5	89.53	50.61	0.9473	0.0066
S2	82.1	2.23	0.9864	0–1	1.7E-4	67.70	20.00	0.9527	0.0106
S3	61.9	0.71	0.9816	0–1	5.9E-4	39.29	8.70	0.9754	0.0154

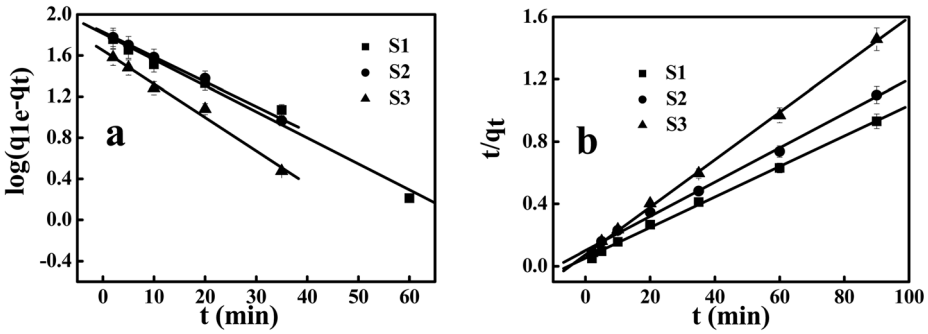

Fig. 5 Adsorption kinetics for the adsorption of Pb^{2+} on Fe_3O_4 NPs (15 mg of adsorbent, initial dye concentration 100 mg L^{-1}, neutral pH, test temperature: 18 °C) (a) pseudo-first order and (b) pseudo-second order.

Table 3 Adsorption parameters obtained from the kinetics for the adsorption Pb^{2+} on Fe_3O_4 NPs

	Pseudo-first-order					Pseudo-second-order			
Adsorbent	K_1 (min^{-1})	q_{1e} (mg g^{-1})	r_1^2	SD	K_2 (g mg^{-1} min^{-1})	q_{2e} (mg g^{-1})	h (mg g^{-1} min^{-1})	r_2^2	SD
S1	0.058	65.23	0.9806	0.0882	0.0018	102.0	19.14	0.9981	0.0153
S2	0.059	76.38	0.9964	0.0225	0.0012	90.9	10.03	0.9966	0.0229
S3	0.075	44.55	0.9874	0.0568	0.0031	65.6	13.51	0.9988	0.0186

(min^{-1}). The adsorption rate constant (K_1) was calculated from the plot of log ($q_{1e} - q_t$) against t.

Ho and McKay[11] presented the pseudo-second-order kinetic as:

$$\frac{t}{q_t} = \frac{1}{K_2 q_{2e}^2} + \frac{t}{q_{2e}} \quad (6)$$

where K_2 is the pseudo-second-order rate constant (g mg^{-1} min^{-1}). The initial adsorption rate, h (mg g^{-1} min^{-1}) at $t \rightarrow 0$ is defined as:

$$h = K_2 q_{2e}^2 \quad (7)$$

where h, q_{2e} and K_2 can be obtained by linear plot of t/q_t *versus* t.

Fig. 5 shows plots of the pseudo-first-order and second-order kinetics of Pb^{2+} adsorption on Fe_3O_4 NPs. The calculated kinetic parameters are given in Table 3. The comparison of correlation coefficients (r^2) of the linearized form of both equations indicates that the kinetic data for the sorbent were fitted to a pseudo-second-order kinetic model. The best fit to the pseudo-second-order kinetics indicates that the adsorption mechanism depends on the adsorbate and adsorbent.

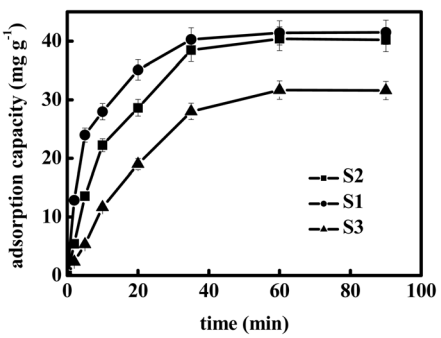

Fig. 6 The adsorption capacity of S1, S2 and S3 for Cr^{6+} removal from water.

Removal of Cr^{6+}

The scheme for the removal of Cr^{6+} from aqueous solution using adsorbents is shown in Fig. 6. Aqueous solutions with an initial Cr^{6+} concentration of 50 mg L^{-1} were used for the experiment at neutral pH = 7, the adsorption time ranged from 0 to 90 min, and T = 18 °C. The equilibrium adsorption capacities of S1 to S3 for Cr^{6+} are 41.5, 40.2 and 31.6 mg g^{-1}, respectively. Similar to the results obtained in Pb^{2+} adsorption, the water-soluble Fe_3O_4 NPs exhibit an excellent adsorption capacity for Cr^{6+}.

Table 4 Adsorption capacities of Pb^{2+} and Cr^{6+} on various adsorbents

Type of adsorbent	q_{max} (mg g^{-1})	Reference
Adsorption of Pb^{2+}		
Manganese oxide coated alumina	58.9	13*a*
Ni@C composite nanostructures	21.4	13*b*
Magnesium silicate hollow nanostructures	64.8	13*c*
Nitrogen-containing activated carbon	56.0	13*d*
Amidoximated bacterial cellulose	67.0	13*e*
Manganese oxide coated zeolite	75.0	13*f*
Magnetic carbonaceous nanoparticles	123.1	13*g*
Modified kaolin	20.0	13*h*
Water-soluble Fe_3O_4 nanoparticles	96.8	Present study
Adsorption of Cr^{6+}		
$Fe@Fe_2O_3$ core-shell nanowires	7.8	13*i*
Magnesium silicate hollow nanostructures	10.3	13*c*
Chitosan modified Fe^0 nanowires	113.2	13*j*
Modified jacobsite	31.5	13*k*
Distillery sludge	5.7	13*l*
Streptomyces rimosus	26.7	13*m*
Iron nanoparticle decorated graphene	162.0	13*n*
Water-soluble Fe_3O_4 nanoparticles	41.5	Present study

Compared with S2, S1 shows a slightly higher adsorption capacity due to its slightly smaller particle sizes. Furthermore, about 30 min after contact, a rapid removal of Cr^{6+} was observed. After 90 min, the adsorption of Cr^{6+} almost reaches saturation.

Mechanism of adsorption

In general conditions, the specific surface area of the adsorbent might be a key point to influence adsorption capacity. In this contribution, the surface charges of products are the most important factors to decide the final adsorption capacity, because the test results of BET show the surface areas of the synthesized adsorbents from S1 to S3 are 50.8, 47.3, and 59.0 m^2 g^{-1}, respectively. On the basis of the FTIR spectra (Fig. 2A), we believe that the surfaces of the as-prepared samples S1 and S2 are coated with carboxyl groups. As a result, the samples show high solubility in water. A large number of carboxyl groups on the surface of magnetite are responsible for its water solubility, which also leads to the increasing surface negative charges on the surface of water-soluble magnetite[12]. Hence, an electrostatic attraction may be the main adsorption mechanism, because the negative charges on the magnetite surface could participate in capturing heavy-metal ions with positive charges. This is also in accordance with a previous report, which demonstrates that the presence of carboxylic functional groups on the surface of colloidal nanoparticles is favorable for the adsorption of heavy-metal ions.[12] Furthermore, one novelty for the application of water-soluble magnetite in the field of sewage water is that the heavy-metal ions can sufficiently contact with water-soluble magnetite. It is likely that the full contact conduces the species to attract each other.

Performance evaluation

The maximum adsorption capacity (q_{max}) for S1 nanoparticles for Cr^{6+} and Pb^{2+} is listed in Table 4 with literature values of q_{max} of other adsorbents for Cr^{6+} and Pb^{2+} adsorption.[13] All of the adsorbents used for Cr^{6+} and Pb^{2+} adsorption have considerably lower q_{max} values than S1 used in this study, except magnetic carbonaceous nanoparticles,[13g] and chitosan modified Fe^0 nanowires.[13j] However, the simplicity of the preparation method, the water solubility and high magnetic response for S1 nanoparticles make them a better adsorbent than the others for the adsorption of heavy-metal ions.

Conclusions

The Langmuir model is favorable to the adsorption process. Adsorption kinetics indicate that the adsorption mechanism depends on the adsorbate and adsorbent. The as-prepared water-soluble Fe_3O_4 nanoparticles with high water solubility and high saturation magnetization (before and after adsorption) show an excellent ability to remove and call back heavy-metal ions. Electrostatic attraction is the adsorption mechanism for the water-soluble Fe_3O_4 NPs.

Acknowledgements

The financial support from the Natural Science Foundation of Jilin Province (20101542) of China and the National Foundation of Doctoral Station (grant No. 20100061110019) are acknowledged.

References

1 (*a*) M. Eloussaief and M. Benzina, *J. Hazard. Mater.*, 2010, **178**, 753; (*b*) V. Javanbakht, H. Zilouei and K. Karimi, *Int. Biodeterior. Biodegrad.*, 2011, **65**, 294; (*c*) S. C. Wu, X. L. Peng, K. C. Cheng, S. L. Liu and M. H. Wong, *Bioresour. Technol.*, 2009, **100**, 4559.
2 (*a*) B. Hu and H. J. Luo, *Appl. Surf. Sci.*, 2010, **257**, 769; (*b*) T. H. Shi, Zh. Ch. Wang, Y. Liu, Sh. G. Jia and Ch. M. Du, *J. Hazard. Mater.*, 2009, **161**, 900; (*c*) A. González, N. Moreno, R. Navia and X. Querol, *Fuel*, 2010, **89**, 3012; (*d*) Y. Q. Lan, Ch. Li, J. D. Mao and J. Sun, *Chemosphere*, 2008, **71**, 781.
3 (*a*) R. Molinari, P. Argurio and T. Poerio, *Desalination*, 2004, **162**, 217; (*b*) S. E. Manaham, *Environmental Chemistry*, CRC Press, Boca Raton, 7th edn, 2000; (*c*) F. Gode and E. Pehlivan, *J. Hazard. Mater.*, 2006, **136**, 330; (*d*) Z. Hu, L. Lei, Y. Li and Y. Ni, *Sep. Purif. Technol.*, 2003, **31**, 13.
4 V. Chandra, J. Park, Y. Chun, J. W. Lee, I. Hwang and S. K. Kim, *ACS Nano*, 2010, **4**, 3979.
5 (*a*) X. Y. Hou, J. Feng, X. H. Liu, Y. M. Ren, Z. J. Fan and M. L. Zhang, *J. Colloid Interface Sci.*, 2011, **353**, 524; (*b*) Ch. Hui, Ch. M. Shen, T. Zh. Yang, L. H. Bao, J. F. Tian, H. Ding, Ch. Li and H. J. Gao, *J. Phys. Chem. C*, 2008, **112**, 11336; (*c*) Z. Li, B. Tan, M. Allix, A. I. Cooper and M. J. Rosseinsky, *Small*, 2008, **4**, 231.
6 W. Cheng, K. B. Tang, Y. X. Qi, J. Sheng and Zh. P. Liu, *J. Mater. Chem.*, 2010, **20**, 1799.
7 X. Ch. Wei, Z. W. Wei, L. P. Zhang, Y. Q. Liu and D. Y. He, *J. Colloid Interface Sci.*, 2011, **354**, 76.
8 H. M. F. Freundlich, *Z. Phys. Chem.*, 1906, **57**, 385.
9 I. Langmuir, *J. Am. Chem. Soc.*, 1918, **40**, 1361.
10 S. Lagergren, *Handlingar*, 1898, **24**, 1.
11 Y. S. Ho and G. McKay, *Process Biochem.*, 1999, **34**, 451.
12 H. Wang, Y. F. Yu, Q. W. Chen and K. Cheng, *Dalton Trans.*, 2011, **40**, 559.
13 (*a*) E. Eren, B. Afsin and Y. Onal, *J. Hazard. Mater.*, 2009, **161**, 677; (*b*) Y. H. Ni, L. N. Jin, L. Zhang and J. M. Hong, *J. Mater. Chem.*, 2010, **20**, 6430; (*c*) Y. Zhuang, Y. Yang, G. L. Xiang and X. Wang, *J. Phys. Chem. C*, 2009, **113**, 10441; (*d*) A. D. Budaeva and E. V. Zoltoev, *Fuel*, 2010, **89**, 2623; (*e*) S. Y. Chen, W. Shen, F. Yu, W. L. Hu and H. P. Wang, *J. Appl. Polym. Sci.*, 2010, **117**, 8; (*f*) W. H. Zou, R. P. Han,

Z. Z. Chen, J. H. Zhang and J. Shi, *Colloids Surf., A*, 2006, **279**, 238; (*g*) I. F. Nata, G. W. Salim and C. K. Lee, *J. Hazard. Mater.*, 2010, **183**, 853; (*h*) M. Q. Jiang, Q. P. Wang, X. Y. Jin and Z. L. Chen, *J. Hazard. Mater.*, 2009, **170**, 332; (*i*) Z. H. Ai, Y. Cheng, L. Z. Zhang and J. R. Qiu, *Environ. Sci. Technol.*, 2008, **42**, 6955; (*j*) L. Sun, L. D. Zhang, C. H. Liang, Z. G. Yuan, Y. Zhang, W. Xu, J. X. Zhang and Y. Z. Chen, *J. Mater. Chem.*, 2011, **21**, 5877; (*k*) J. Hu, I. M. C. Lo and G. H. Chen, *Langmuir*, 2005, **21**, 11173; (*l*) K. Selvaraj, S. Manonmani and S. Pattabhi, *Bioresour. Technol.*, 2003, **89**, 207; (*m*) A. Chergui, M. Z. Bakhti, A. Chahboub, S. Haddoum, A. Selatnia and G. A. Junter, *Desalination*, 2007, **206**, 179; (*n*) H. Jabeen, V. Chandra, S. Jung, J. W. Lee, K. S. Kim and S. B. Kim, *Nanoscale*, 2011, **3**, 3583.